Journal of Materials Chemistry A

ROYAL SOCIETY OF CHEMISTRY

COMMUNICATION

View Article Online
View Journal | View Issue

Cite this: J. Mater. Chem. A, 2025, 13, 19282

Received 1st April 2025
Accepted 2nd June 2025

DOI: 10.1039/d5ta02572a

rsc.li/materials-a

A self-assembled monolayer as a hole-transport layer forming a robust interface with the active layer for enhanced thermal stability in organic solar cells†

Yelim Choi,[a] Yurim Bae,[a] Haeryang Lim,[a] Hangyeol Kim,[a] Dawoon Kim,[b] Dayeong Choi,[a] Minjun Kim,*[c] Taiho Park *[a] and Sung Yun Son *[b]

Can self-assembled monolayer (SAM)-based hole transport layers (HTLs) overcome the interfacial instability issues associated with PEDOT:PSS and offer a more robust platform for charge extraction, both mechanically and electrically? This work provides a rationale for the improved thermal and interfacial stability of the SAM HTL in organic solar cells.

Organic solar cells (OSCs), particularly those based on bulk heterojunctions of donor polymers and non-fullerene acceptors, have achieved power conversion efficiencies (PCEs) exceeding 19%.[1–3] These advances are driven not only by material innovation and device optimization but also by progress in interface engineering.[4–8]

In conventional OSCs (p-i-n configuration), the hole-transport layer (HTL) positioned between the active layer and the indium tin oxide (ITO) electrode is essential for ensuring efficient charge extraction.[9–12] An optimal HTL establishes an ohmic contact with the electrode, and selectively facilitates hole transport while blocking electrons.[13,14] Poly(3,4-ethylenedioxythiophene):polystyrene sulfonate (PEDOT:PSS) remains the most widely used HTL due to its commercial availability, suitable energy level alignment, and electron-blocking properties.[15–19] Recently, self-assembled monolayers (SAMs) have emerged as promising alternatives, offering favorable energy levels, high transparency, and minimal material consumption.[20–28]

Despite the distinct physical and chemical properties of PEDOT:PSS and SAMs, direct comparisons of the interfaces they form with active layers—particularly regarding interfacial stability—are limited. In this study, we present a representative comparison between the active layer and two different HTLs: PEDOT:PSS and a SAM. We further investigate the impact of thermal annealing on these interfacial properties to provide exemplary insight into their thermal stability.

MeO-functionalized [2-(9*H*-carbazol-9-yl)ethyl]phosphonic acid (MeO-2PACz) was employed as the SAM-based HTL due to its surface energy and energy levels being comparable to those of PEDOT:PSS. PM6 and Y6 were selected as the donor and acceptor materials, respectively, for the active layer. The chemical structures are presented in Fig. S1.†

To evaluate the robustness of each HTL/active layer interface before and after thermal annealing, we performed a peeling test. PM6:Y6 blend films were coated onto either MeO-2PACz or PEDOT:PSS, followed by the application of 3 M adhesive tape. The tape was then detached using a universal testing

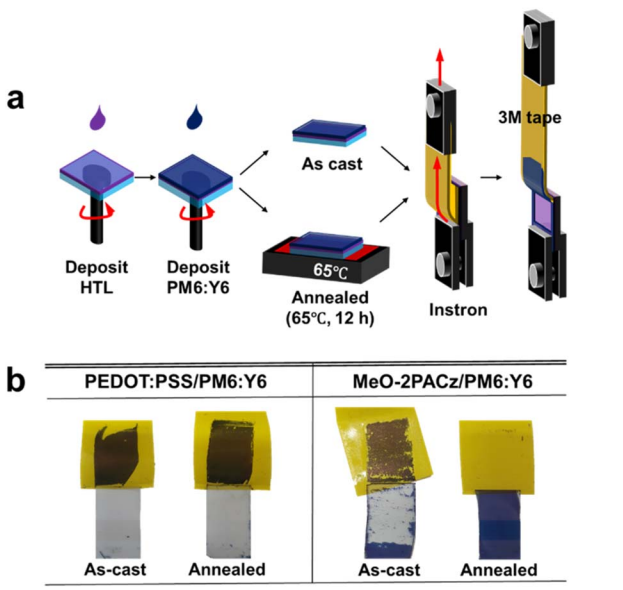

Fig. 1 (a) Schematic representation of the peeling test procedure. (b) Photographs of the PEDOT:PSS/PM6:Y6 and MeO-2PACz/PM6:Y6 films after the peeling test.

[a]Department of Chemical Engineering, Pohang University of Science and Technology, Pohang, Gyeongbuk, 37673, Republic of Korea
[b]Department of Chemistry, Kwangwoon University, Seoul, 01897, Republic of Korea
[c]Department of Chemistry, Kyonggi University, Kyonggi, 16227, Republic of Korea

† Electronic supplementary information (ESI) available. See DOI: https://doi.org/10.1039/d5ta02572a

machine.[29–31] The detailed methodology is illustrated in Fig. 1a, and the entire procedure is demonstrated in the ESI Videos (Videos S1–S4).† Thermal annealing was performed at 65 °C, well below the reported glass transition temperatures (T_g) of PM6 (~115 °C) and Y6 (~102 °C),[32,33] in order to minimize morphological changes in the active layer that might influence the HTL/active layer interface. Indeed, grazing-incidence wide-angle X-ray scattering (GIWAXS) analysis confirmed that no morphological changes occurred during 12 hours of annealing at this temperature (Fig. S2 and S3†).

Fig. 1b presents images of the samples after the peeling test. In PEDOT:PSS/PM6:Y6 samples, the PM6:Y6 layer was completely peeled off in both as-cast and annealed films. MeO-2PACz/PM6:Y6 as-cast films showed significant detachment, with only a few areas remaining intact. In contrast, in the annealed MeO-2PACz/PM6:Y6 film, the PM6:Y6 layer remained fully adhered, showing no visible detachment.

The results of the peeling test were further validated by UV-vis absorption spectroscopy. For PEDOT:PSS/PM6:Y6 samples, the absorption spectra of both as-cast and annealed films significantly decreased after peeling, indicating removal of the PM6:Y6 layer (Fig. S4a†). A similar trend was observed for the as-cast MeO-2PACz/PM6:Y6 sample (Fig. S4b†). In contrast, the annealed MeO-2PACz/PM6:Y6 sample showed negligible change in its absorption spectrum after peeling, confirming that the active layer remained intact.

To determine whether the peeling process removed only the active layer or both the active layer and HTL, we performed Raman imaging and energy-dispersive X-ray spectroscopy (EDS). Line-scan Raman imaging of PEDOT:PSS/PM6:Y6 samples before and after peeling indicated that mainly the active layer was removed (Fig. S5†). In the case of MeO-2PACz, no distinct Raman signals were detected, so EDS elemental mapping was employed. The comparison of EDS maps before and after peeling confirmed that only the active layer was removed in the as-cast MeO-2PACz/PM6:Y6 sample as well (Fig. S6†). These results indicate that thermal annealing improves the interfacial adhesion between MeO-2PACz and the active layer, whereas PEDOT:PSS fails to form a robust interface even after annealing.

Further insight into the difference in adhesion is obtained by measuring the contact angle to estimate the interfacial energy (γ) and Flory–Huggins interaction parameter (χ).[34,35] The measured contact angles are summarized in Table S1,† while interfacial energy and χ values are presented in Table 1.

Table 1 Interfacial energy (γ) and Flory–Huggins parameter (χ) of the PEDOT:PSS/PM6:Y6 and MeO-2PACz/PM6:Y6 interface before and after thermal annealing

Sample	Condition	χ	γ [mN m^{-1}]
PEDOT:PSS/PM6:Y6	As cast	48.7	29.0
	Annealed	21.0	38.5
MeO-2PACz/PM6:Y6	As cast	5.3	55.3
	Annealed	6.8	13.3

Upon thermal annealing, the two systems exhibited contrasting trends: PEDOT:PSS/PM6:Y6 showed an increase in γ (29.0 → 38.5 mN m^{-1}) and a decrease in χ (48.7 → 21.0), whereas MeO-2PACz/PM6:Y6 exhibited a marked decrease in γ (55.3 → 13.3 mN m^{-1}) and a slight increase in χ (5.3 → 6.8). While these values provide useful approximations, it should be noted that contact angle-based estimations primarily reflect surface properties and may not fully capture the morphological and chemical changes occurring at buried interfaces upon annealing. Nevertheless, given that a lower interfacial energy generally reflects stronger thermodynamic favorability and adhesion at the interface, these findings are consistent with the peeling test results and suggest that MeO-2PACz forms a more favorable and stable interface with the active layer after thermal annealing, whereas the PEDOT:PSS interface becomes relatively less compatible.

Subsequently, depth-profile X-ray photoelectron spectroscopy (XPS) was performed to gain deeper insight into the molecular-level changes at the HTL/active layer interface induced by thermal annealing. The full set of spectra is presented in Fig. S7,† while a summary graph showing the peak positions at each depth is provided in Fig. 2a–d. The elements representing each layer were selected based on their chemical structures: F 1s was used to track the PM6:Y6 layer, S 2p (from the sulfonic acid group) for PEDOT:PSS, and P 2p for MeO-2PACz. Additionally, C 1s and In 3d signals were analyzed to track the ITO substrate and assess possible indium diffusion into the active layer.[34,35]

In the as-cast PEDOT:PSS/PM6:Y6 sample, a mixed region of approximately 20 nm was observed between the active layer and the HTL, indicating interfacial interpenetration (Fig. 2a). After thermal annealing, this mixed region was significantly reduced to ~5 nm (Fig. 2b), suggesting phase separation between PEDOT:PSS and PM6:Y6.

In contrast, depth-profile XPS analysis of the MeO-2PACz/PM6:Y6 sample revealed distinctly different interfacial characteristics. Prior to thermal annealing, no measurable overlap was detected between the active layer and the HTL (Fig. 2c), indicating the formation of a well-defined interface. Upon thermal annealing, however, slight interfacial overlap was observed (Fig. 2d), implying the formation of closer physical contact between MeO-2PACz and PM6:Y6.

These observations are schematically illustrated in Fig. 2e to highlight the differences in molecular behavior at the interface induced by thermal annealing. Since the active layer was deposited *via* a solution process onto the HTL, the resulting interface is initially kinetically trapped. In the case of PEDOT:PSS, partial mixing occurs at the interface in the as-cast state, but limited miscibility results in phase separation upon annealing. Conversely, in the MeO-2PACz system, thermal annealing promotes closer physical contact with the active layer, leading to enhanced adhesion.

Given that these differences in interfacial morphology may affect charge transfer at the HTL/active layer interface, charge carrier mobility was evaluated using space-charge limited current (SCLC) measurements. To eliminate contributions from

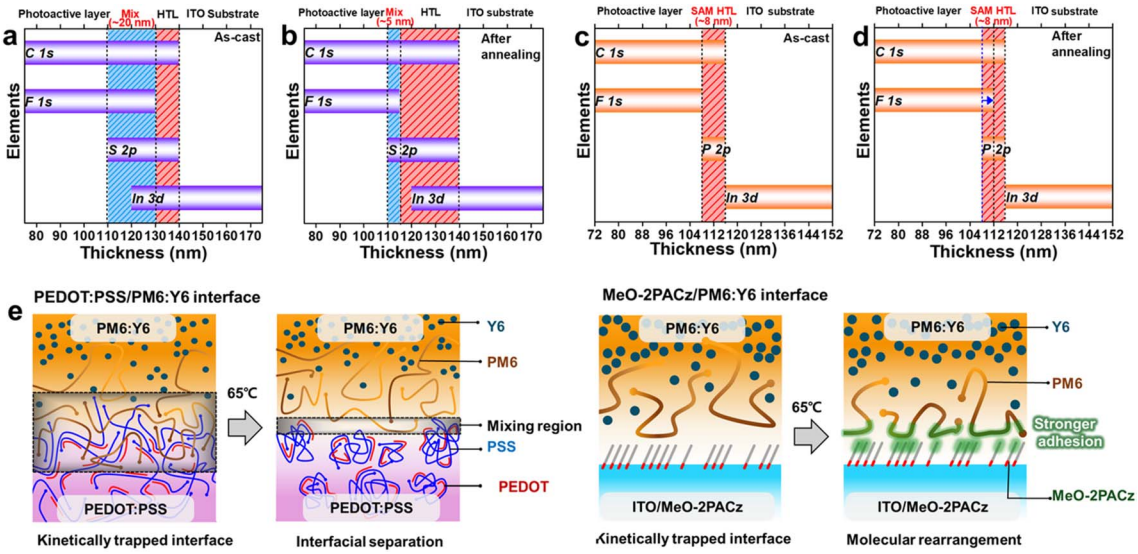

Fig. 2 Summary of the peak presence and chart based on depth-profile XPS data of the (a) as-cast ITO/PEDOT:PSS/PM6:Y6 film and (b) annealed ITO/PEDOT:PSS/PM6:Y6 film at 65 °C for 12 hours, and (c) as-cast ITO/MeO-2PACz/PM6:Y6 film and (d) annealed ITO/Meo-2PACz/PM6:Y6 film at 65 °C for 12 hours. (e) Schematic illustration of proposed molecular arrangements at the PEDOT:PSS/PM6:Y6 and MeO-2PACz/PM6:Y6 interfaces after thermal annealing.

the donor/acceptor interface in the bulk heterojunction, a simplified device structure (ITO/HTL/PM6/Ag) was employed.

As the excessive thickness of the PM6 layer can promote exciton recombination prior to charge extraction, the film deposition conditions were optimized by adjusting the concentration of the PM6 solution. Time-resolved photoluminescence (TRPL) measurements confirmed that a concentration of 0.5 mg ml^{-1} yielded an optimal film thickness for reliable SCLC characterization (Fig. S8†). Using this optimized condition, negligible changes in hole mobility were observed in the ITO/PM6/Ag control device after thermal annealing at 65 °C for 12 hours (from 4.16×10^{-4} to 4.39×10^{-4} cm^2 V^{-1} s^{-1}) (Fig. S9a†)

Subsequently, SCLC measurements were conducted on devices incorporating HTLs. A significant reduction in hole mobility was observed in PEDOT:PSS-based devices after thermal annealing (from 9.55×10^{-4} to 3.51×10^{-4} cm^2 V^{-1} s^{-1}) (Fig. S9b†), whereas MeO-2PACz-based devices maintained mobility under the same thermal conditions (6.91×10^{-4} to 7.05×10^{-4} cm^2 V^{-1} s^{-1}) (Fig. S9c†).

To further investigate interfacial charge recombination, electrochemical impedance spectroscopy (EIS) was performed under illumination. Measurements were carried out under open-circuit voltage conditions across the frequency range of 7 MHz to 10 Hz, and the results were plotted as Nyquist diagrams (Fig. 3a).[36–39] The extracted resistance values are summarized in Table 2. The series resistance (R_1), which accounts for the resistance of the ITO/HTL interface, wire resistance, and electrode sheet resistance, was comparable for both systems regardless of before and after thermal annealing. However, clear differences were observed in the interfacial resistance (R_2), which reflects charge transfer resistance at the PM6:Y6 and HTL/PM6:Y6 interfaces.

After thermal annealing, the R_2 value for PEDOT:PSS-based devices increased substantially from 19.6 Ω to 111 Ω, whereas the increase for the MeO-2PACz-based device was relatively low

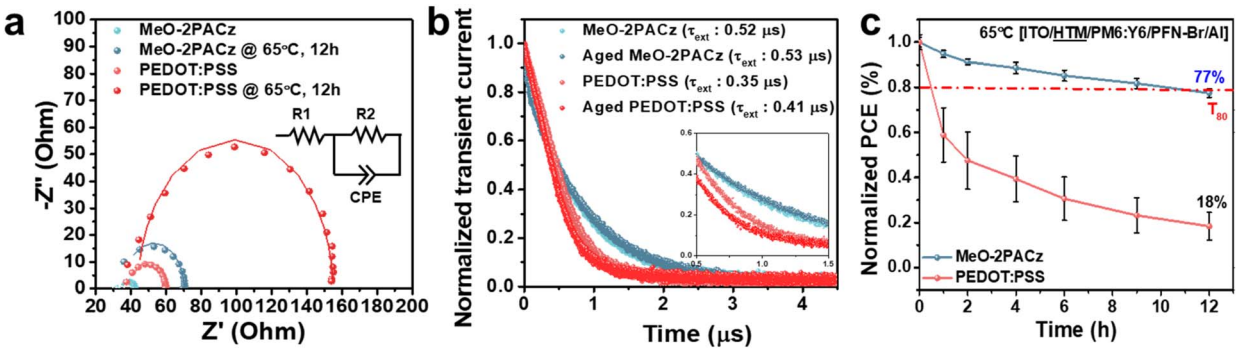

Fig. 3 (a) Nyquist plots of the ITO/HTL/PM6:Y6/Ag devices measured under one sun illumination and open-circuit voltage conditions. (b) TPC responses of ITO/HTL/PM6:Y6/Ag devices. (c) Thermal stability of 10 different devices incorporating MeO-2PACz or PEDOT:PSS as the HTL, monitored over 12 hours at 65 °C under a nitrogen atmosphere.

Table 2 Fitting parameters of the impedance spectra with an equivalent circuit model

HTL[a]	Condition	R_1 (Ω)	R_2 (Ω)
PEDOT:PSS	As-cast	40.0	19.6
	Annealed	44.0	111
MeO-2PACz	As-cast	36.3	5.83
	Annealed	36.0	34.1

[a] Device structures of ITO/HTL/PM6:Y6/Ag.

(from 5.83 Ω to 34.1 Ω). Given that the PM6:Y6 blend morphology remained largely unchanged under these thermal conditions, the observed increase in R_2 is attributed primarily to degradation at the HTL/active layer interface.

Next, transient photocurrent (TPC) measurements were also carried out to assess charge-carrier extraction dynamics (Fig. 3b). Devices were fabricated with the structure ITO/HTL/PM6:Y6/Ag to exclude the influence of electron transport layers and isolate the contribution of the HTL to extraction behavior. Under pulsed illumination, photogenerated carriers were generated and collected at the HTL. The extraction time (τ_{ext}), which reflects recombination at interfacial defect sites, was analyzed. For PEDOT:PSS-based devices, τ_{ext} increased from 0.35 μs to 0.41 μs after thermal annealing, indicating that charge extraction is hindered after thermal annealing. Conversely, the MeO-2PACz-based devices almost maintained the τ_{ext} (0.52 to 0.53 μs), confirming robust charge extraction properties (see Note S1† for discussion on the non-ideal decay behavior and interpretation of τ_{ext} values).[40–43]

These results collectively indicate that MeO-2PACz forms a mechanically and electrically stable interface with the PM6:Y6 active layer under 65 °C annealing conditions. In contrast, the PEDOT:PSS interface undergoes phase separation and degradation, leading to deteriorated charge transfer.

Finally, the thermal stability of complete OSCs was evaluated by monitoring PCE under a nitrogen atmosphere at 65 °C for 12 hours. The initial device efficiencies are summarized in Table S3.† After 12 hours at 65 °C, the PEDOT:PSS-based device retained only 18% of its initial PCE, while the MeO-2PACz-based device preserved 77%. The raw data corresponding to these results are summarized in Table S4,† and the *J–V* degradation behavior of the device exhibiting the highest PCE retention is presented in Fig. S10.† It is worth noting that no additional device optimization was performed. This result clearly demonstrates that the use of MeO-2PACz as the HTL results in significantly improved thermal stability.

Conclusions

Interfacial stability plays a critical role in the thermal durability of organic solar cells (OSCs). In this study, we systematically investigated the mechanical and electrical robustness of the interfaces formed between PM6:Y6 and two representative hole-transport layers (HTLs): PEDOT:PSS and MeO-2PACz. Thermal annealing was found to induce phase separation at the PEDOT:PSS interface, resulting in increased charge transfer resistance. In contrast, MeO-2PACz maintained a well-defined and stable interface even after thermal treatment.

A combination of mechanical (peeling test), spectroscopic (XPS, Raman, and EDS), and electrical (SCLC, EIS, and TPC) characterization studies revealed that MeO-2PACz forms a thermally resilient interface with the active layer. Notably, MeO-2PACz-based OSCs retained 77% of their initial power conversion efficiency after 12 hours at 65 °C, whereas PEDOT:PSS-based devices degraded rapidly, retaining only 18%.

These results highlight the importance of interfacial design in achieving stable OSC performance and demonstrate that SAM-based HTLs such as MeO-2PACz offer a promising pathway toward thermally robust and efficient organic photovoltaics.

Data availability

The data supporting the findings of this study are available from the corresponding author upon reasonable request.

Conflicts of interest

There are no conflicts to declare.

Acknowledgements

In situ GIWAXS measurements were performed using synchrotron radiation on the 9A beamline at the Pohang Accelerator Laboratory (PAL), Korea. This work was supported by the National Research Foundation of Korea (NRF) grant funded by the Korean government (MSIT) (No. 2021R1A2C3004420 and No. 2021R1A5A1084921), and by the Korea Institute of Energy Technology Evaluation and Planning (KETEP) grant funded by the Korean government (MOTIE) (RS-2024-00451343).

Notes and references

1 X. Zhou, C. Gu, C. Zheng, B. Liu, Y. Tian, H. Yang and X. Bao, *J. of Mater. Chem. A*, 2024, **12**, 19839–19860.
2 H. Liang, K. Ma, S. Ding, W. Zhao, X. Si, X. Cao and Y. Chen, *Adv. Energy Mater.*, 2024, **14**, 2402370.
3 Y. Li, Z. Ge, L. Mei, H. Ma, Y. Chen, X. Wang and Y. Sun, *Angew. Chem.*, 2024, **136**, e202411044.
4 M. Casademont-Viñas, D. Capolat, A. Quesada-Ramírez, M. Reinfelds, G. Trimmel, M. Sanviti and M. Campoy-Quiles, *J. of Mater. Chem. A*, 2024, **12**, 16716–16728.
5 M. Choi, H. S. Jeong, J. Lee, Y. Choi, I. B. Kim, D. Y. Kim, S. Y. Jang and J. of, *Mater. Chem. A*, 2024, **12**, 8963–8971.
6 Y. Choi, S. A. Park, Y. Bae, D. Kim, M. Kim and T. Park, *Adv. Opt. Mater.*, 2023, **11**, 2201788.
7 Y. Bae, S. A. Park, S. Kim, H. Lim, J. Kim, L. Ye and T. Park, *Adv. Energy Mater.*, 2025, **15**, 2405217.
8 S. Y. Son, J. W. Kim, J. Lee, G. W. Kim, J. Hong, J. Y. Kim and T. Park, *J. Mater. Chem. A*, 2018, **6**, 24580–24587.
9 Y.-C. Chin, M. Daboczi, C. Henderson, J. Luke and J.-S. Kim, *ACS energy letters*, 2022, **7**, 560–568.

10 J. Xu, A. Späth, W. Gruber, A. Barabash, P. Stadler, K. Gubanov and T. Heumüller, *Nano energy*, 2023, **118**, 108956.
11 D. G. Romero, G. Bontekoe, J. Pinna, L. Di Mario, C. M. Ibarra-Barreno, J. Kardula and M. A. Loi, *Adv. Energy Mater.*, 2025, 2404981.
12 F. Wang, Z. a. Tan and Y. Li, *Energy Environ. Sci.*, 2015, **8**, 1059–1091.
13 Y. C. Chin, M. Daboczi, C. Henderson, J. Luke and J. S. Kim, *ACS Energy Lett.*, 2022, **7**, 560–568.
14 F. Z. Wang, Z. A. Tan and Y. F. Li, *Energy Environ. Sci.*, 2015, **8**, 1059–1091.
15 Y. Lee, S. Biswas and H. Kim, *Thin Solid Films*, 2022, **746**, 139134.
16 J. Lee, J.-W. Lee, H. Song, M. Song, J. Park, G.-U. Kim, D. Jeong, T.-S. Kim and B. J. Kim, *J. Mater. Chem. A*, 2023, **11**, 12846–12855.
17 M. Raïssi, S. Wageh, A. A. Al-Ghamdi and D. Rousseau, *J. Mater. Chem. A*, 2023, **11**, 25578–25594.
18 S. U. Ryu, D. H. Lee, Z. U. Rehman, J.-C. Lee, H. Lim, G. Shin, C. E. Song and T. Park, *Chem. Eng. J.*, 2024, **485**, 149865.
19 H. Zheng, L. Hu, X. Hu, H. Li, J. Quan, Y. Jin, X. Yin, J. Song, Z. Su and D. Zhou, *J. Mater. Chem. A*, 2024, **12**, 2413–2422.
20 A. Al-Ashouri, A. Magomedov, M. Ross, M. Jost, M. Talaikis, G. Chistiakova, T. Bertram, J. A. Márquez, E. Köhnen, E. Kasparavicius, S. Levcenco, L. Gil-Escrig, C. J. Hages, R. Schlatmann, B. Rech, T. Malinauskas, T. Unold, C. A. Kaufmann, L. Korte, G. Niaura, V. Getautis and S. Albrecht, *Energy Environ. Sci.*, 2019, **12**, 3356–3369.
21 H. L. Cheng, Y. G. Li and Y. F. Zhong, *Mater. Chem. Front.*, 2023, **7**, 3958–3985.
22 R. Geng, P. Liu, R. Pan, H. Xu, S. Gao, Z. Zhang, T. Su, H. Wu, W. Zhu and X. Song, *Chem. Eng. J.*, 2023, **454**, 140138.
23 D. A. González, C. E. P. Galvis, W. Li, M. Méndez, E. Aktas, E. Martínez-Ferrero and E. Palomares, *Nanoscale Adv*, 2023, **5**, 6542–6547.
24 J. Jing, S. Dong, K. Zhang, B. Xie, J. Zhang, Y. Song and F. Huang, *Nano Energy*, 2022, **93**, 106814.
25 Y. Lin, Y. Firdaus, F. H. Isikgor, M. I. Nugraha, E. Yengel, G. T. Harrison, R. Hallani, A. El-Labban, H. Faber and C. Ma, *ACS Energy Lett.*, 2020, **5**, 2935–2944.
26 Y. Lin, A. Magomedov, Y. Firdaus, D. Kaltsas, A. El-Labban, H. Faber, D. R. Naphade, E. Yengel, X. Zheng and E. Yarali, *ChemSusChem*, 2021, **14**, 3569–3578.
27 Y. Lin, Y. Zhang, J. Zhang, M. Marcinskas, T. Malinauskas, A. Magomedov, M. I. Nugraha, D. Kaltsas, D. R. Naphade and G. T. Harrison, *Adv. Energy Mater.*, 2022, **12**, 2202503.
28 W. Wang, Z. Lin, S. Gao, W. Zhu, X. Song and W. Tang, *Adv. Funct. Mater.*, 2023, **33**, 2303653.
29 W. Greenbank, N. Rolston, E. Destouesse, G. Wantz, L. Hirsch, R. Dauskardt and S. Chambon, *J. Mater. Chem. A*, 2017, **5**, 2911–2919.
30 L. C. Tan, Y. L. Wang, J. W. Zhang, S. Q. Xiao, H. Y. Zhou, Y. W. Li, Y. W. Chen and Y. F. Li, *Adv. Sci.*, 2019, **6**, 1801180.
31 S. Yu and C. Cha, *Macromol. Res.*, 2023, **31**, 427–441.
32 Y. H. Kim, C. Sachse, M. L. Machala, C. May, L. Müller-Meskamp and K. Leo, *Adv. Funct. Mater.*, 2011, **21**, 1076–1081.
33 Q. L. Zhang, Y. Z. Chen, X. J. Liu and M. Fahlman, *J. Mater. Chem. C*, 2023, **11**, 3112–3118.
34 Q. An, J. Wang, X. Ma, J. Gao, Z. Hu, B. Liu, H. Sun, X. Guo, X. Zhang and F. Zhang, *Energy Environ. Sci.*, 2020, **13**, 5039–5047.
35 Y. X. Li, B. Huang, X. N. Zhang, J. W. Ding, Y. Y. Zhang, L. E. Xiao, B. X. Wang, Q. Cheng, G. S. Huang, H. Zhang, Y. G. Yang, X. Y. Qi, Q. Zheng, Y. Zhang, X. H. Qiu, M. H. Liang and H. Q. Zhou, *Nat. Commun.*, 2023, **14**, 1241.
36 M. J. Jin, J. Jo and J. W. Yoo, *Org. Electron.*, 2015, **19**, 83–91.
37 Q. Liao, Q. Kang, Y. Yang, C. An, B. Xu and J. Hou, *Adv. Mater.*, 2020, **32**, e1906557.
38 H. S. Park, Y. W. Han, H. S. Lee, S. J. Jeon and D. K. Moon, *ACS Appl. Energy Mater.*, 2020, **3**, 3745–3754.
39 Y. Zhang, L. R. Li, S. S. Yuan, G. Q. Li and W. F. Zhang, *Electrochim. Acta*, 2013, **109**, 221–225.
40 C. G. Shuttle, B. O'Regan, A. M. Ballantyne, J. Nelson, D. D. Bradley, J. De Mello and J. R. Durrant, *Appl. Phys. Lett.*, 2008, **92**, 093311.
41 H. Yu, Y. Wang, X. Zou, J. Yin, X. Shi, Y. Li and S. Chen, *Nat. Commun.*, 2023, **14**, 2323.
42 J. Fu, Q. Yang, P. Huang, S. Chung, K. Cho, Z. Kan and G. Li, *Nat. Commun.*, 2024, **15**, 1830.
43 S. Wood, J. C. Blakesley and F. A. Castro, *Phys. Rev. Appl.*, 2018, **10**, 024038.

